# MINISTRY OF EDUCATION AND TRAINING

# VIETNAM ACADEMY OF SCIENCE AND TECHNOLOGY

#### GRADUATE UNIVERSITY OF SCIENCE AND TECHNOLOGY



#### Vu Van Thuy

# SYNTHESIS OF PRUSSIAN BLUE ANALOGUE MATERIALS (MHCF, M = Fe, Ni, Co, Ce) FOR SUPERCAPACITOR ELECTRODE APPLICATIONS

SUMMARY OF DISSERTATION ON SCIENCES OF MATTER
Major: Inorganic Chemistry
Code: 9 44 01 13

The dissertation is completed at: Graduate University of Science and Technology, Vietnam Academy Science and Technology

#### Supervisors:

- 1. Supervisor 1: Assoc Prof. Dr. Tran Viet Thu Military Technology Academy, Ministry of Defense.
- 2. Supervisor 2: Dr. Nguyen Si Hieu Institute of Materials Science, Vietnam Academy of Science and Technology.

Referee 1:

Referee 2:

Referee 3:

The dissertation can be found at:

- 1. Graduate University of Science and Technology Library
- 2. National Library

#### INTRODUCTION

## 1. The urgency of the dissertation

Global warming and the depletion of fossil fuels have become increasingly serious concerns in recent years, promoting the transition toward the use of green energy sources. The utilization of solar, wind, and hydrogen energy not only requires energy conversion devices - such as solar cells and water-splitting systems - but also necessitates the development of efficient energy storage devices due to the intermittent nature of these energy sources. In recent years, various materials have been investigated for this purpose, among which Prussian Blue (PB) and Prussian Blue Analogues (PBAs) have attracted considerable attention.

Prussian Blue is ferric ferrocyanide (Fe<sub>4</sub><sup>3+</sup>[Fe<sup>2+</sup>(CN)<sub>6</sub>]<sub>3</sub>), which contains only one type of metal in its composition. It can be synthesized by reacting Fe<sup>3+</sup> solution with [Fe<sup>2+</sup>(CN)<sub>6</sub>]<sup>4-</sup> or Fe<sup>2+</sup> with [Fe<sup>3+</sup>(CN)<sub>6</sub>]<sup>3-</sup>. When the Fe metal is replaced by other transition metals, compounds with structures similar to Prussian Blue are obtained, generally represented as A<sub>x</sub>T[M(CN)<sub>6</sub>], where A = Li, K, Na; T = Fe, Co, Mn, Cu, ...; and M = Fe, Mn, Co, ... These compounds are collectively referred to as Prussian Blue Analogues (PBAs). PBAs possess an open framework structure, which facilitates the insertion and extraction of metal ions into and out of the crystal lattice. The lattice structure undergoes minimal distortion during repeated ion insertion/extraction processes. Furthermore, their composition can be easily tuned, offering flexibility in performance, controllable morphology, and adjustable structural complexity. Owing to these advantages, PBAs have been widely investigated as promising electrode materials for batteries and supercapacitors. In addition, PBAs can be synthesized using relatively simple and versatile methods with abundant and low-cost precursors.

In Vietnam, mastering the development of electrochemical energy conversion and storage devices is of great importance in the near future. As a first step, it is essential to focus on the synthesis of electrode materials and to gain an in-depth understanding of the operating mechanisms of both the materials and the associated devices. Therefore, the selection of the dissertation topic entitled "sythesis of prussian blue analogue materials (MHCF, M = Fe, Ni, Co, Ce) for supercapacitor electrode applications" is both necessary and highly significant in terms of scientific and practical relevance.

#### 2. Research objectives of the dissertation

- Analyze the composition, structure, and characteristic properties of Prussian Blue (PB) and Prussian Blue Analogues (PBAs). Review and evaluate various synthesis methods of PBAs, clarifying the procedures, advantages, disadvantages, and application scopes of each method. On this basis, establish a foundation for selecting an appropriate synthesis approach suitable for the laboratory conditions and the objectives of this dissertation.
- Synthesize material systems based on hexacyanoferrate compounds, and investigate their structural, physicochemical, and electrochemical properties. Based on these findings, design supercapacitor devices that are appropriate for energy conversion and storage applications.
- Study the factors influencing the performance of supercapacitors, including the composition and structure of electrode materials, the type of electrolyte, and the operating conditions, in order to determine the optimal parameters for fabricating a simple electrochemical energy storage device.

#### 3. Research content of the dissertation

- Study, synthesize, and investigate the electrochemical properties of cerium hexacyanoferrate(II).
- Investigate the electrochemical behavior of FeHCF synthesized by the co-precipitation method for potassium-ion  $(K^+)$  storage applications.
- Synthesize nickel/cobalt hexacyanoferrate(III) and study its application as an electrode material for aqueous asymmetric hybrid supercapacitors.
- Synthesize sodium-rich nickel/cobalt hexacyanoferrate(II) to enhance the performance of aqueous electrochemical energy storage devices.

#### **CHAPTER 1. OVERVIEW**

Chapter 1 comprises 28 pages and presents a comprehensive literature review on Prussian Blue and Prussian Blue Analogues (PBAs), including their composition, structure, synthesis methods, and applications. It also summarizes recent studies on MHCF (M = Fe, Co, Ni, Ce) material systems and provides an overview of the operating mechanisms of supercapacitors.

#### CHAPTER 2. RESEARCH METHODS AND EXPERIENCE

Chapter 2 consists of 10 pages and provides a detailed description of the synthesis methods for each material system. It also presents the characterization techniques used to evaluate the material properties, such as XRD, EDX, XPS, FT-IR, TGA, SEM, and TEM. In addition, this chapter introduces the electrochemical characterization methods, including CV, GCD, and EIS, as well as the procedures for fabricating supercapacitor devices using the synthesized materials and evaluating their performance.

#### **CHAPTER 3. RESULTS AND DISCUSSION**

# 3.1. Investigation of the properties of CeHCF

#### 3.1.1. Characterization of CeHCF

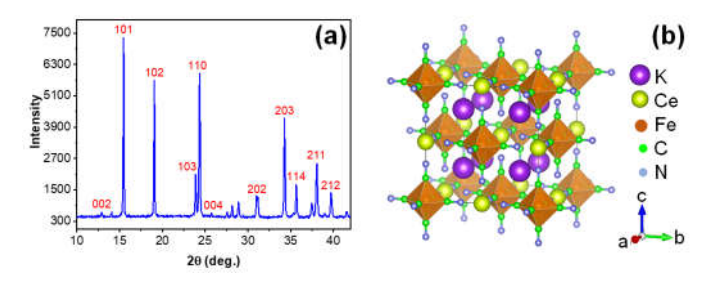


Figure 3.1. XRD pattern (a) and simulated crystal structure (b) of CeHCF.

The powder X-ray diffraction (XRD) pattern of CeHCF (Figure 3.1a) exhibits characteristic diffraction peaks corresponding to KCe[Fe(CN)<sub>6</sub>], which crystallizes in a hexagonal structure (space group P6<sub>3</sub>/m; JCPDS card No. 83-2292).

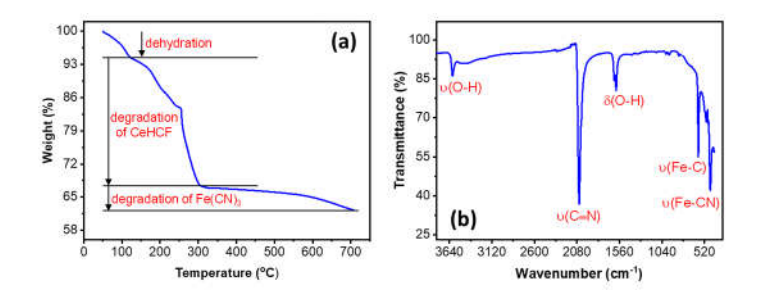


Figure 3.2. TGA (a) and FT-IR (b) spectra of CeHCF

The TGA and FT-IR analyses further confirm the successful synthesis of CeHCF.

The SEM image of the as-synthesized CeHCF particles (Figure 3.3) reveals a uniform morphology resembling Christmas trees, with most of the particles having submicrometer dimensions.

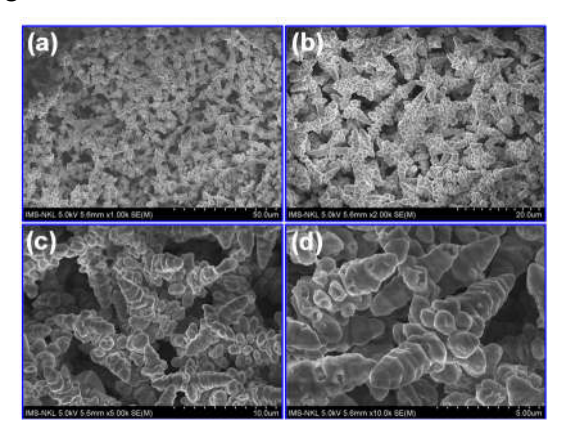


Figure 3.3. (a–d) SEM images of CeHCF.

The SEM–EDX spectrum (Figure 3.4) confirmed the presence of Ce (2.92 at%), Fe (2.23 at%), C (44.87 at%), N (47.44 at%), and K (2.54 at%) elements in the as-synthesized CeHCF. The atomic ratio of Ce to Fe was calculated to be 2.92:2.23  $\approx$  4:3, which is consistent with the theoretical stoichiometry of Ce<sub>4</sub>[Fe(CN)<sub>6</sub>]<sub>3</sub>.

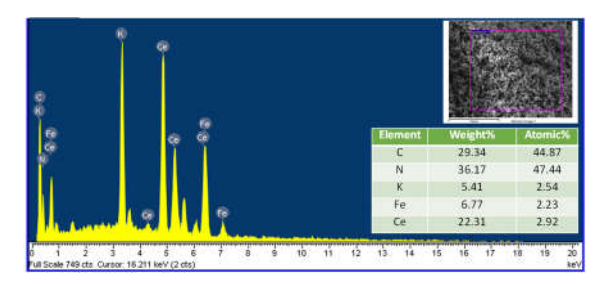


Figure 3.4. EDX spectrum of CeHCF. Inset: SEM image (top) and elemental composition of CeHCF (bottom).

#### 3.1.2. Electrochemical properties of CeHCF

The shapes of the CV curves exhibit distinct but not sharp oxidation and reduction peaks, with a potential difference of approximately 0.1 V, indicating that the electrochemical mechanism is a pseudocapacitive intercalation process. Therefore, the charge storage capacity should be expressed in units of F g<sup>-1</sup>. As observed, each CV curve displays two distinguishable cathodic peaks, which can be attributed to the electrochemical reduction of  $\text{Ce}^{4+}/\text{Ce}^{3+}$  and  $[\text{Fe}^{3+}(\text{CN})_6]^{3-}/[\text{Fe}^{2+}(\text{CN})_6]^{4-}$  redox couples. These reduction processes are likely accompanied by the intercalation of K<sup>+</sup> ions. In contrast, only one anodic peak is observed, which may result from the overlapping of the two corresponding oxidation processes.

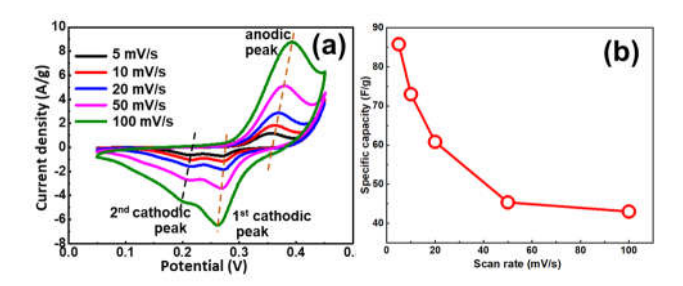


Figure 3.5. CV curves (a) and specific capacitance (Cs) calculated from CV of CeHCF.

The capacitance of CeHCF is relatively low compared to other HCF materials, which may be attributed to its hexagonal crystal structure with lattice parameters of a = 7.35 Å and c = 13.86 Å. The relatively small lattice dimensions are unfavorable for the intercalation of  $K^+$  ions during the charge–discharge process.

The shapes of the GCD curves also reflect the pseudocapacitive intercalation nature of CeHCF in electrochemical energy storage. At high charge–discharge rates, the charge and discharge curves are relatively symmetrical and form a nearly triangular shape. When the charge–discharge rate decreases, the curves split into two distinct regions: the upper part at higher potentials shows a linear and relatively symmetric charge–discharge profile, while the lower part at lower potentials exhibits a potential plateau region. As shown in Figure 3.7(b), when the current density decreases from 0.8 to 0.1 A g<sup>-1</sup>, the specific capacitance (Cs) increases from 51.9 to 96.0 F g<sup>-1</sup>, which is consistent with the values obtained from the CV analysis.

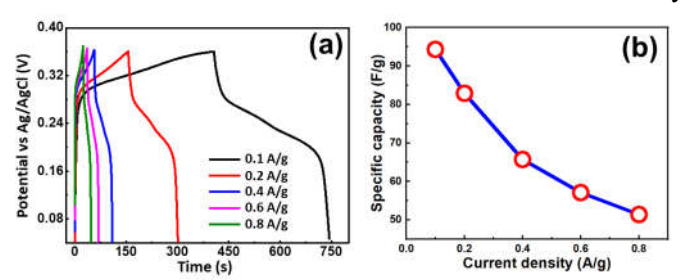


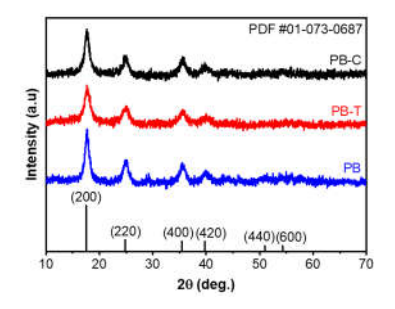
Figure 3.7. GCD curves (a) and Cs calculated from GCD (b) of CeHCF.

The specific capacitance of CeHCF is relatively low, making it less suitable for practical applications in energy conversion and storage. Subsequent studies are therefore directed toward other material systems with higher specific capacitance, starting with the parent Prussian Blue compound in which both transition metal sites are occupied by Fe.

#### 3.2. Investigation of the properties of FeHCF

#### 3.2.1. Characterization of FeHCF

As shown in Figure 3.8, the XRD patterns of FeHCF, PB-T, PB-C, and PB exhibit strong diffraction peaks at approximately 17.76°, 25.05°, 35.56°, and 39.99°, which correspond to the (200), (220), (400), and (420) crystal planes, respectively, of the face-centered cubic (fcc) phase (space group Fm3m) of iron cyanide hydrate (PDF #01-073-0687).



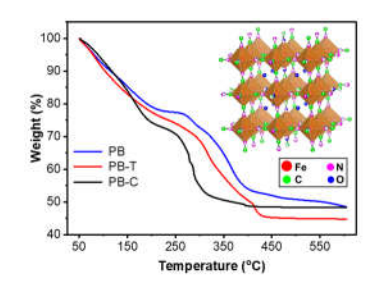


Figure 3.8. XRD patterns of PB, PB-T, and PB-C.

Figure 3.9. TGA curves of PB, PB-T, and PB-C.

From the TGA profiles, the amount of water released from PB is the smallest among the three samples, indicating that PB contains a lower water content, which has been demonstrated to be beneficial for its electrochemical performance.

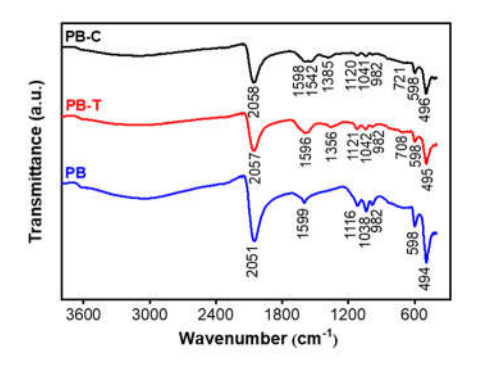


Figure 3.10. FT-IR spectra of PB, PB-T, and PB-C
The FT-IR spectra clearly exhibit all the characteristic bonds of the

hexacyanoferrate family. The SEM images reveal that the primary small cubic particles tend to aggregate, forming larger secondary structures.

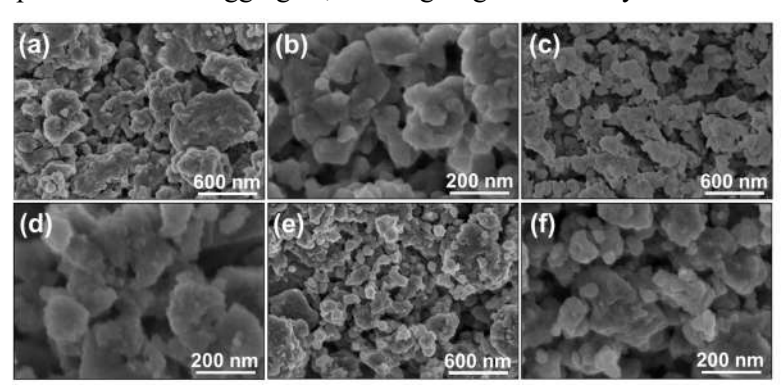


Figure 3.11. SEM images of PB-T (a-b), PB-C (c-d), and PB (e-f).

# 3.2.2. Electrochemical properties of FeHCF

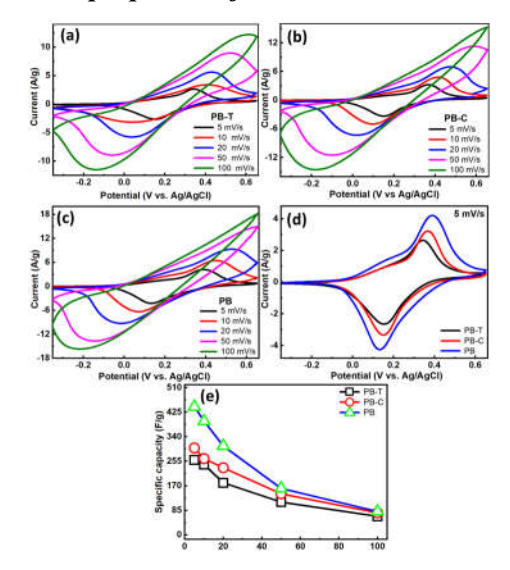


Figure 3.12. CVs of PB-T (a), PB-C (b), and PB (c); CV curves measured at 5 mV/s (d); Cs as a function of scan rate (e)

All CV curves of PB-T, PB-C, and PB (Figures 3.12a-c) exhibit a pair

of redox peaks, attributed to the intercalation and deintercalation of  $K^+$  ions. At the same scan rate, both the peak-to-peak separation and the absolute current density of PB are higher than those of PB-C and PB-T, as shown in Figure 3.12d (at a scan rate of 5 mV·s<sup>-1</sup>). The specific capacitance (Cs) of PB, calculated at the same scan rate, is also higher than that of PB-C and PB-T (Figure 3.12e). The calculated Cs values of PB-T, PB-C, and PB at a scan rate of 5 mV·s<sup>-1</sup> are 272.9, 316.2, and 466.0 F·g<sup>-1</sup>, respectively.

The stable potential region observed during the discharge process corresponds well with the peak potentials observed in the CV curves, confirming the intercalation-type pseudocapacitive behavior of the synthesized material. A comparison of the GCD profiles for all three samples, measured at a current density of  $1 \text{ A} \cdot \text{g}^{-1}$  (Figure 3.14d), shows that the calculated specific capacitance (Cs) of PB is 193 F·g<sup>-1</sup>, significantly higher than that of PB-T (113 F·g<sup>-1</sup>) and PB-C (105 F·g<sup>-1</sup>). The Cs of PB also exceeds those of PB-T and PB-C at other current densities (Figure 3.15a), consistent with the CV analysis.

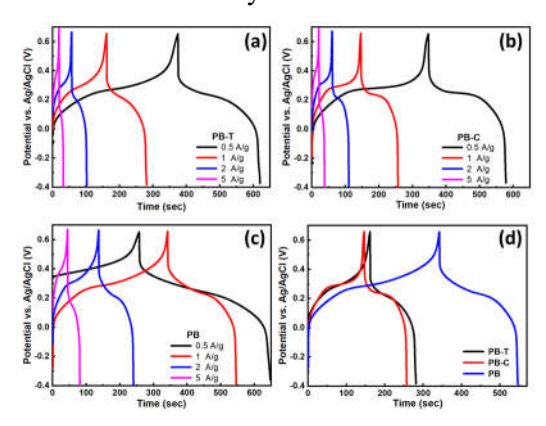


Figure 3.14. GCD profiles of PB-T, PB-C, and PB at different current densities (a-c) and at a current density of  $I \land g^{-1}(d)$ .

# 3.2.3. Electrochemical properties of devices constructed from FeHCF

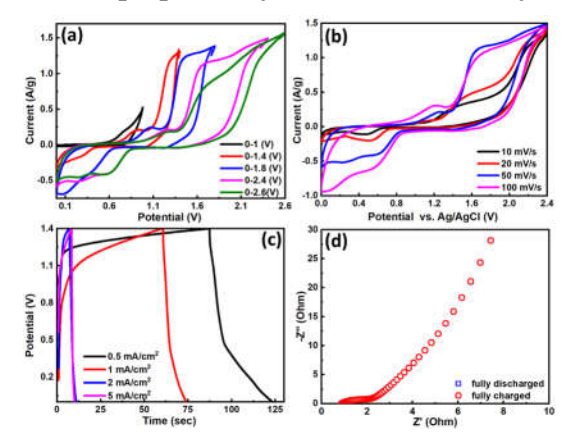


Figure 3.16. Electrochemical performance of the assembled test device: (a–b) CV curves at different potential windows and scan rates; (c) GCD profiles at various current densities; and (d) EIS spectra of the device in fully charged and fully discharged states

The specific capacitance values of PB materials as well as the devices are not yet sufficiently outstanding to be considered for practical applications. Therefore, in the following section of this dissertation, the author investigates alternative material systems based on hexacyanoferrate with the aim of enhancing the electrochemical performance. Among these approaches, the incorporation of other transition metals (Ni, Co) to partially substitute Fe in the PB structure represents a research direction that demonstrates significant potential.

#### 3.3. Investigation of the properties of Ni<sub>x</sub>Co<sub>y</sub>HCF

# 3.3.1. Characterization of Ni<sub>x</sub>Co<sub>y</sub>HCF

The XRD patterns fully confirm the successful synthesis of Ni<sub>1</sub>Co<sub>2</sub>HCF. As the Co content increases, the diffraction peaks gradually shift toward higher 2θ values (Figure 3.17(b)), resulting in a decrease in the interplanar spacing. This phenomenon can be attributed to the difference in ionic radii between Ni<sup>2+</sup> and Co<sup>2+</sup> ions when substituting for Fe<sup>3+</sup> ions in the crystal lattice.

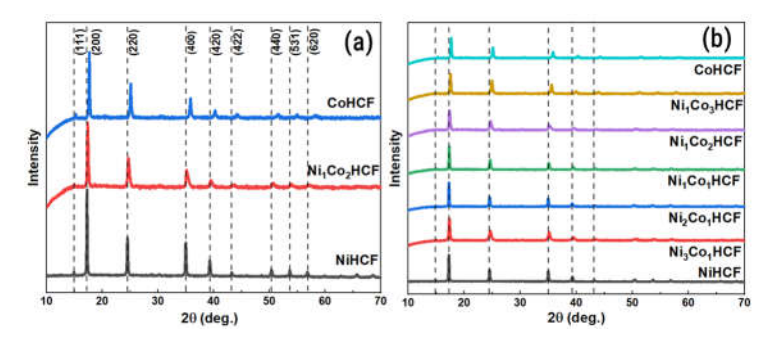


Figure 3.17. XRD patterns of NixCoyHCF(III).

The TGA and FT-IR spectra of NixCoyHCF are similar to those of the previously studied FeHCF. Interestingly, the FT-IR spectra (Figure 3.18(d)) reveal clear differences corresponding to the Ni:Co ratios in the samples. As the Co content increases, the absorption peak around 2100 cm<sup>-1</sup> becomes more pronounced, whereas the absorption peak near 2160 cm<sup>-1</sup> is enhanced with higher Ni content..

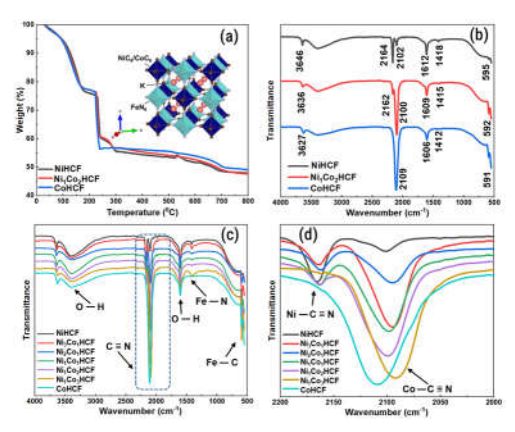


Figure 3.18. TGA (a) and FT-IR spectra (b, c, d) of NixCoyHCF(III).

Figures 3.19(a–c) present SEM and TEM images of the Ni<sub>1</sub>Co<sub>2</sub>HCF sample, which exhibits well-crystallized micro- or nanosized cubic structures with smooth surfaces. The particle size of Ni<sub>1</sub>Co<sub>2</sub>HCF is approximately 100 nm, significantly smaller than those reported in previous studies.

The SEM images and corresponding SEM-EDS elemental mapping of Ni<sub>1</sub>Co<sub>2</sub>HCF, shown in Figures 3.19(d–e), confirm the uniform distribution of the relevant elements (Ni, Co, Fe, C, N, and K) throughout the micro-sized particles.

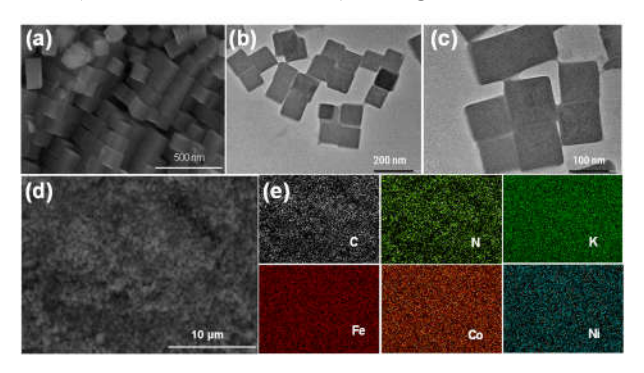


Figure 3.19. SEM image (a) and TEM images (b, c) of Ni<sub>1</sub>Co<sub>2</sub>HCF; SEM mapping image (d) and SEM-EDS elemental mapping (e) of Ni<sub>1</sub>Co<sub>2</sub>HCF.

# 3.3.2. Electrochemical properties of Ni<sub>x</sub>Co<sub>y</sub> HCF

All CV curves exhibit a pair of redox peaks corresponding to the insertion/extraction of K<sup>+</sup> ions into/from the crystal lattice. The anodic peak current (Ipa) of CoHCF appears at a higher potential than that of NiHCF, while both cathodic peak currents (Ipc) are observed in similar potential regions. The CV curves of NiHCF, CoHCF, and NixCoyHCF with different Ni:Co molar ratios, recorded at a scan rate of 50 mV s<sup>-1</sup>, are shown in Figure 3.20(d). Among the samples, Ni<sub>1</sub>Co<sub>2</sub>HCF exhibits the largest peak-to-peak separation, peak current, and enclosed area, indicating the highest specific capacitance and suggesting that the optimal Ni:Co molar ratio is 1:2. The redox peaks are well-defined but not sharp, with a potential difference of approximately 0.15 V between the anodic and cathodic peaks at a scan rate of 10 mV s<sup>-1</sup>, confirming that the charge storage mechanism of NixCoyHCF follows an intercalation-type pseudocapacitive behavior. Compared with PB, the NixCoyHCF samples display broader (less sharp) redox peaks and smaller potential separations between oxidation and reduction peaks. This indicates faster K<sup>+</sup> ion insertion/extraction kinetics and better reversibility, which contribute to the enhanced electrochemical performance.

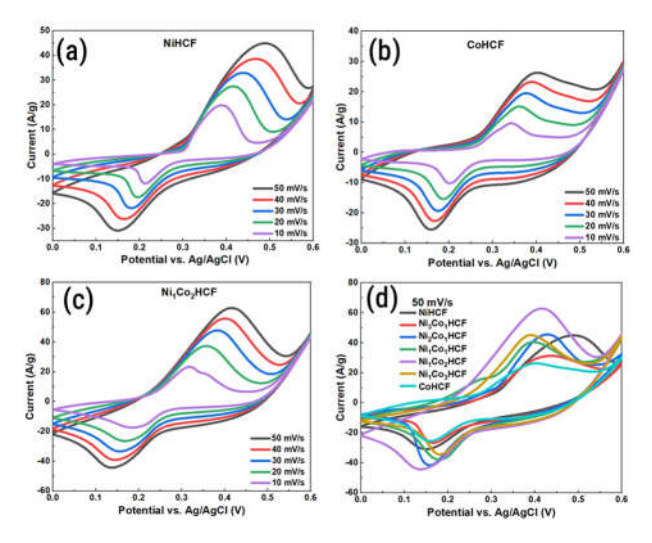


Figure 3.20. CV curves of NiHCF (a), CoHCF (b), and Ni<sub>1</sub>Co<sub>2</sub>HCF (c) recorded at different scan rates, and CV curves of NixCoyHCF at a scan rate of 50 mV s<sup>-1</sup>.

The Randles–Sevcik plots of NiHCF, CoHCF, and Ni<sub>1</sub>Co<sub>2</sub>HCF (Figure 3.21(a)) exhibit a linear relationship between Ipa and Ipc with  $\sqrt{\nu}$ , with a high correlation coefficient of 0.99. In contrast, when the correlation between Ipa and Ipc and  $\nu$  is plotted, the linear correlation coefficient decreases to 0.96 (Figure 3.21(b)). These results indicate that their electrochemical behavior is governed by a semi-infinite diffusion-controlled intercalation-type pseudocapacitive process. The relationship between current (I) and scan rate ( $\nu$ ) can be expressed by Equation (3.5): I =  $\nu$  In general, the parameter b ranges between 0.5 and 1.0; a value of b close to 0.5 suggests a diffusion-controlled process, whereas a value approaching 1.0 indicates that the kinetics of the surface-controlled process play the dominant role.

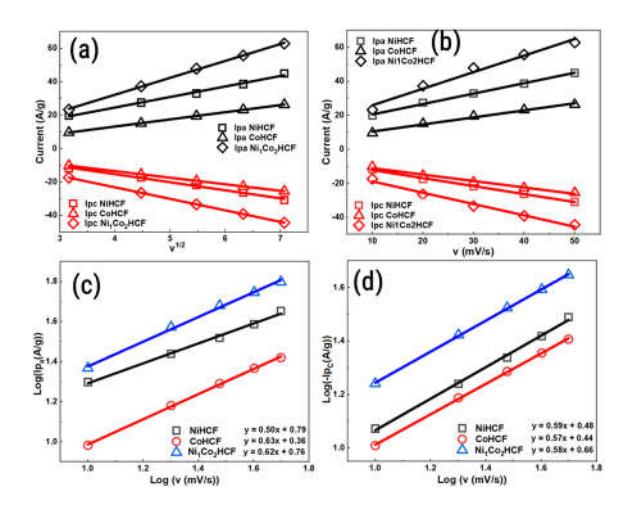


Figure 3.21. Randles—Sevcik plots of Ipa and Ipc versus  $v^{1/2}(a)$ ; Randles—Sevcik plots of Ipa and Ipc versus v(b); plots of log(Ipa) versus log(v)(c); and plots of log(Ipc) versus log(v)(d).

As shown in Figure 3.22(a), the electrochemical behavior of Ni<sub>1</sub>Co<sub>2</sub>HCF is predominantly governed by a diffusion-controlled process. The diffusion contribution decreases, while the capacitive contribution increases with increasing scan rate (Figure 3.22(b)). A similar trend is observed for NiHCF and CoHCF, as illustrated in Figures 3.22(c–d).

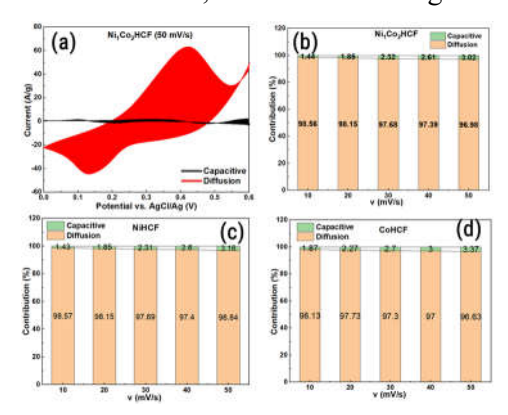


Figure 3.22. Power contribution analysis of Ni<sub>1</sub>Co<sub>2</sub>HCF (a-b), NiHCF (c), and CoHCF (d).

The GCD curves of the synthesized samples are presented in Figures 3.23(a–c). The stable potential plateaus observed in the discharge branches of these GCD profiles correspond well with the redox peak potentials observed in the CV curves, indicating an intercalation-type pseudocapacitive behavior. As shown in Figure 3.23(d), the charge storage capacity of Ni<sub>1</sub>Co<sub>2</sub>HCF is superior to that of NiHCF, CoHCF, and other NixCoyHCF samples with different Ni:Co molar ratios.

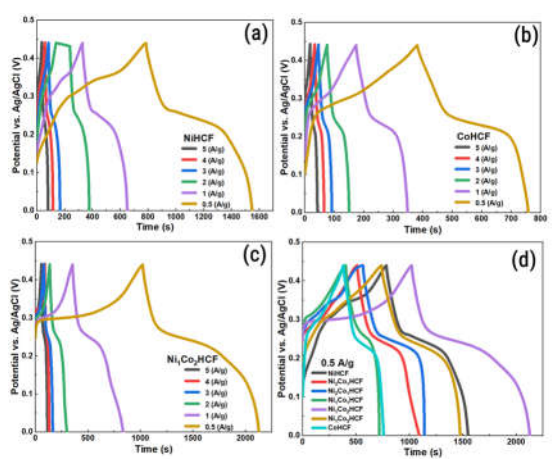


Figure 3.23. GCD curves of NiHCF (a), CoHCF (b), and Ni<sub>1</sub>Co<sub>2</sub>HCF (c); and GCD profiles at a current density of 0.5 A g<sup>-1</sup> (d)

### 3.3.3. Electrochemical properties of devices constructed from Ni<sub>x</sub>Co<sub>y</sub>HCF

The CV curve of the device (Figure 3.25(b)) exhibits an approximately rectangular shape, indicative of pseudocapacitive characteristics. Although the CV curves show slight distortion at higher scan rates—suggesting limited ion diffusion—the device still maintains good capacitive behavior, highlighting its potential for high-power applications. The GCD curves of the device (Figure 3.25(c)) display a noticeable IR drop at higher current densities, indicating increased resistive losses.

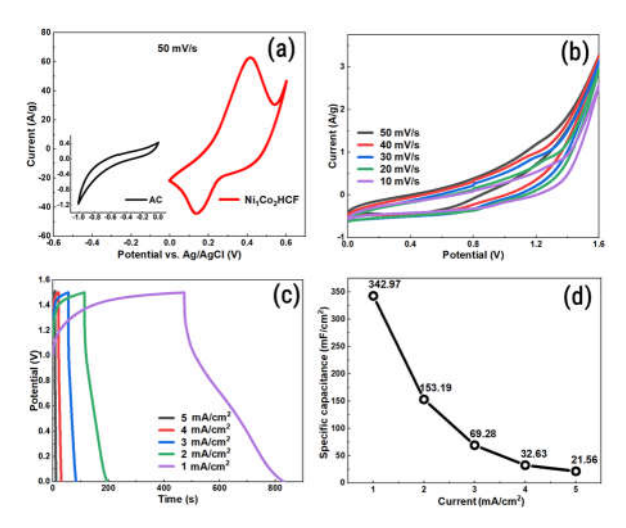


Figure 3.25. (a) CV curves of AC and  $Ni_1Co_2HCF$  at a scan rate of 50 mV  $s^{-1}$ . Electrochemical performance of the assembled device: (b) CV curves; (c) GCD profiles; and (d) dependence of Cs on current density.

Figure 3.26(a) demonstrates that the fabricated device achieves a superior areal performance compared with recently reported materials. Figure 3.26(b) illustrates the cycling stability of the device tested at a current density of 5 mA cm<sup>-2</sup>. The device retains 87.7% of its initial capacitance after 2000 cycles, indicating excellent long-term stability and durability, which can be attributed to the robust electrode material and the stable electrochemical environment within the device. The Nyquist plots recorded at the initial and after 2000 cycles (inset in Figure 3.26(b)) show a very small charge-transfer resistance (Rct) and a nearly vertical line in the low-frequency region, indicative of good capacitive behavior. The slight increase in Rct after 2000 cycles suggests a minor rise in internal resistance, further confirming the stability and reliability of the device. Overall, these electrochemical characteristics demonstrate a well-balanced performance with high energy and power densities, as well as excellent cycling stability.

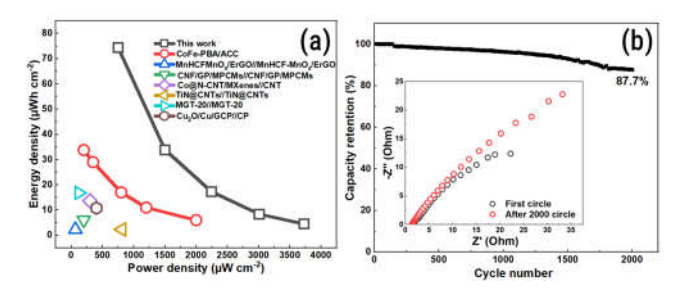


Figure 3.26. (a) Ragone plot of the assembled device; (b) cycling stability at a current density of 5 mA cm<sup>-2</sup>. Inset: EIS spectra recorded at the initial cycle and after 2000 cycles.

To improve the electrochemical performance, in addition to modifying the material composition, the use of suitable electrolytes represents another promising research direction. In the subsequent study, this dissertation employs an electrolyte containing Na<sup>+</sup> ions instead of the previously used K<sup>+</sup>-based electrolytes.

# 3.4. Investigation of the properties of Ni<sub>x</sub>Co<sub>y</sub>HCF rich Na<sup>+</sup>

#### 3.4.1. Characterization of Ni<sub>x</sub>Co<sub>v</sub>HCF rich Na<sup>+</sup>

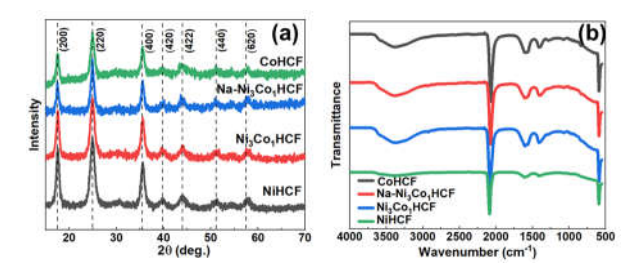


Figure 3.27. (a) XRD patterns and (b) FT-IR spectra of NiHCF, CoHCF, Ni<sub>3</sub>Co<sub>1</sub>HCF, and Na–Ni<sub>3</sub>Co<sub>1</sub>HCF.

As shown in Figure 3.27(a), all samples exhibit characteristic diffraction peaks corresponding to a face-centered cubic (fcc) structure typical of Prussian blue analogues (PBAs). A comparison between the diffraction patterns of Ni<sub>3</sub>Co<sub>1</sub>HCF and Na-Ni<sub>3</sub>Co<sub>1</sub>HCF reveals that the incorporation of Na<sup>+</sup>ions does not significantly alter the crystal

structure or crystallite size of Ni<sub>2</sub>Co<sub>1</sub>HCF, as evidenced by the nearly identical positions and widths of the major diffraction peaks. This observation also indicates that the octahedral interstitial sites within the crystal lattice are sufficiently large to accommodate a considerable amount of Na<sup>+</sup> ions without disturbing the structural framework.

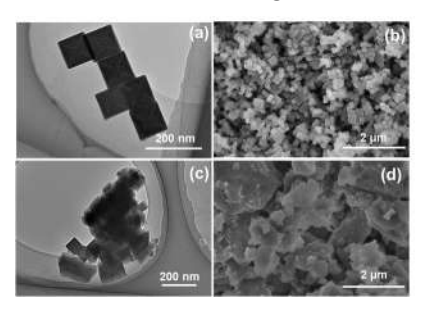


Figure 3.28. TEM and SEM images of Ni<sub>3</sub>Co<sub>1</sub>HCF (a, b); TEM and SEM images of Na–Ni<sub>3</sub>Co<sub>1</sub>HCF (c, d).

The TEM image of Ni<sub>3</sub>Co<sub>1</sub>HCF (Figure 3.28(a)) displays well-defined small cubic particles with an average size of approximately 100–120 nm and high crystallinity. The SEM image of Ni<sub>3</sub>Co<sub>1</sub>HCF (Figure 3.28(b)) reveals uniformly distributed particles that are densely packed, which is advantageous for electrochemical applications owing to the increased active surface area. The TEM and SEM images of Na–Ni<sub>3</sub>Co<sub>1</sub>HCF (Figure 3.28(c–d)) show that, although some smaller cubic particles can still be observed, most particles exhibit varying degrees of aggregation, which may result in the formation of more porous channels compared to Ni<sub>3</sub>Co<sub>1</sub>HCF, thereby facilitating ion diffusion during cycling.

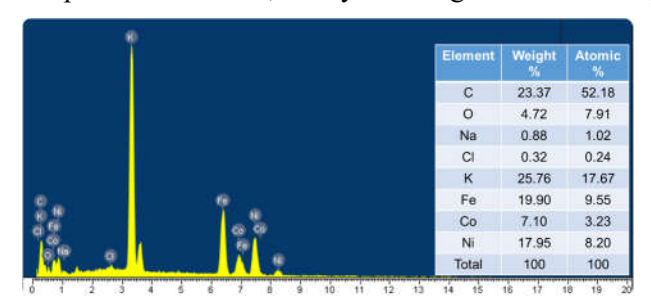


Figure 3.29. EDX spectrum of Na-Ni<sub>3</sub>Co<sub>1</sub>HCF.

The EDX spectrum of Na–Ni<sub>3</sub>Co<sub>1</sub>HCF (Figure 3.29) reveals the presence of Na, K, Ni, Co, Fe, N, O, and Cl elements as minor impurities. Compared with Ni<sub>3</sub>Co<sub>1</sub>HCF, the Na–Ni<sub>3</sub>Co<sub>1</sub>HCF sample exhibits a similar Ni:Co molar ratio of 2.56, a higher content of transition metals (Ni, Co, Fe) and [Fe(CN)<sub>6</sub>] vacancies, as well as a higher alkali metal content and a lower amount of crystal water.

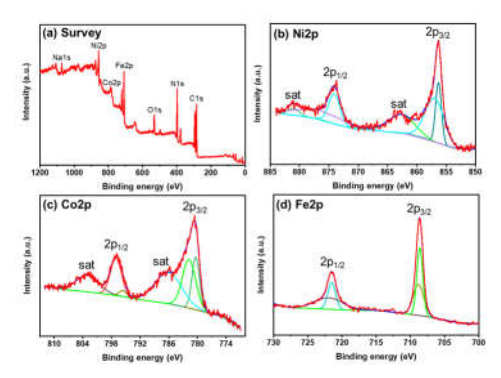


Figure 3.30. XPS spectra of Na–Ni<sub>3</sub>Co<sub>1</sub>HCF

Figure 3.30(a) shows the survey XPS spectrum of the Na–Ni<sub>3</sub>Co<sub>1</sub>HCF sample, indicating the presence of all expected elements (Na, Ni, Co, Fe, O, C, and N) without detectable impurities. The elemental composition of Na–Ni<sub>3</sub>Co<sub>1</sub>HCF obtained from the XPS data is consistent with that derived from the EDX results, confirming that all transition metals are present in the +2 oxidation state.

# 3.4.2. Electrochemical properties of Ni<sub>x</sub>Co<sub>y</sub>HCF rich Na<sup>+</sup>

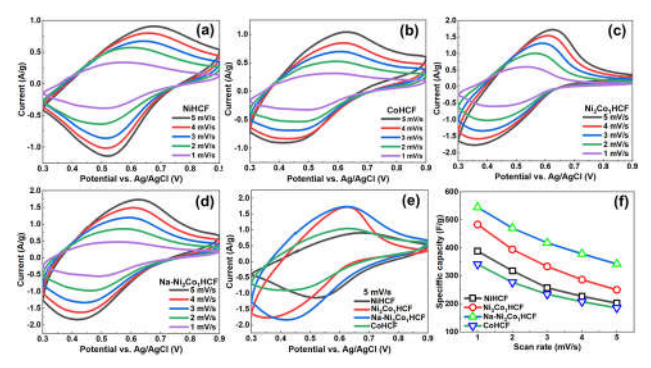


Figure 3.31. Cyclic voltammetry (CV) curves of NiHCF (a), CoHCF (b), Ni<sub>3</sub>Co<sub>1</sub>HCF (c), and Na–Ni<sub>3</sub>Co<sub>1</sub>HCF (d). (e) Comparison of CV profiles for all materials at a scan rate of  $5 \text{ mV s}^{-1}$ ; (f) Cs values as a function of scan rate.

The cyclic voltammetry (CV) profiles of the materials show well-resolved and distinct redox peaks, corresponding to the Ni<sup>2+</sup>/Ni<sup>3+</sup>, Co<sup>2+</sup>/Co<sup>3+</sup>, and Fe<sup>2+</sup>/Fe<sup>3+</sup> redox couples, which, however, cannot be individually distinguished in the CV spectra. Instead, a single broad and overlapping redox pair is observed for all samples. This phenomenon can be attributed to the electrochemical inactivity of the Ni<sup>2+</sup>/Ni<sup>3+</sup> couple within the aqueous electrolyte potential window employed in this study. Therefore, the redox activity of the synthesized samples is mainly associated with the Fe<sup>2+</sup>/Fe<sup>3+</sup> centers coordinated to cyanide ligands, while the nickel and cobalt centers may function as structural or electronic modulators that stabilize the framework, tune the electron density around the iron centers, and influence ion transport properties.

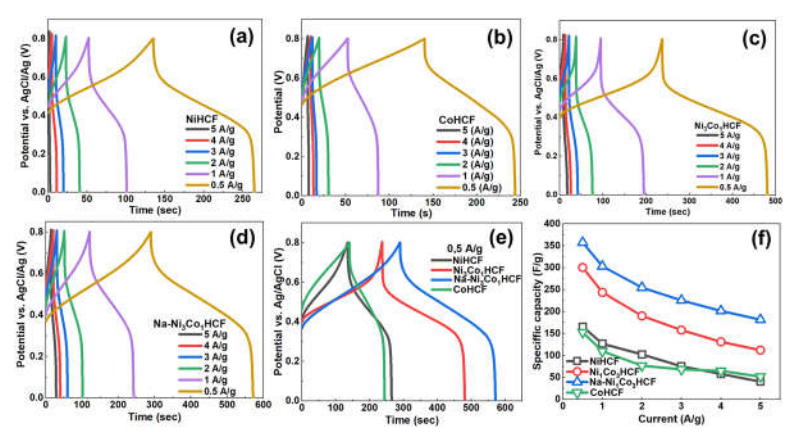


Figure 3.34. GCD curves of NiHCF (a), CoHCF (b), Ni<sub>3</sub>Co<sub>1</sub>HCF (c), and Na–Ni<sub>3</sub>Co<sub>1</sub>HCF (d); (e) GCD curves of all materials at a current density of 0.5 A g<sup>-1</sup>; (f) rate capability; and (g, h) EIS spectra of all materials.

A direct comparison of all materials at a current density of 0.5 A g<sup>-1</sup> (Figure

3.34(e)) clearly shows that Na–Ni<sub>3</sub>Co<sub>1</sub>HCF exhibits the longest charge–discharge duration, which is consistent with the CV analysis. The specific capacitance (Cs) values of the different materials at various current densities (0.5–5 A g<sup>-1</sup>) are presented in Figure 3.34(f). As observed, the Cs of Na–Ni<sub>3</sub>Co<sub>1</sub>HCF is significantly higher than that of the other samples, indicating a remarkable improvement in electrochemical performance resulting from the synergistic effect of Ni<sup>2+</sup> and Co<sup>2+</sup> incorporation as well as the presence of Na<sup>+</sup> ions.

#### 3.4.3. Electrochemical properties of devices constructed from Na-Ni<sub>3</sub>Co<sub>1</sub>HCF

The CV curves of the assembled device (Figure 3.35(b)) highlight its pseudocapacitive characteristics, as evidenced by the nearly rectangular shape of the profiles. Although slight distortions are observed at higher scan rates due to limited ion diffusion, the device maintains good capacitive behavior, demonstrating its suitability for high-power applications. The GCD profiles (Figure 3.35(c)) exhibit a noticeable IR drop at higher current densities, indicating increased resistive losses. Figure 3.35(d) shows the relationship between the areal specific capacitance of the device and the current density.

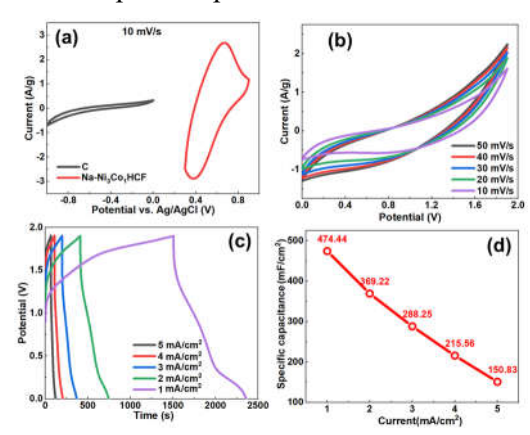


Figure 3.35. (a) CV curves of activated carbon (C) and Na–Ni<sub>3</sub>Co<sub>1</sub>HCF at 10 mV s<sup>-1</sup>; electrochemical performance of the device: (b) CV curves; (c) GCD curves; (d) areal specific capacitance (Cs) as a function of current density.

#### CONCLUSIONS AND RECOMMENDATIONS

With the objective of synthesizing and optimizing the application of MHCF-based material systems, this dissertation has accomplished the following tasks:

- 1.  $Ce_3[Fe(CN)_6]_4$  was successfully synthesized via the reaction between  $Ce^{3+}$  and  $[Fe(CN)_6]_4^{4-}$  ions at room temperature. The as-prepared  $Ce_3[Fe(CN)_6]_4$  exhibited high crystallinity with a hexagonal structure and a uniform submicron "Christmas tree–like" morphology. The synthesized CeHCF demonstrated intercalation-type pseudocapacitive behavior for  $K^+$  storage in an aqueous electrolyte, delivering a specific capacitance of 85.8 F  $g^{-1}$  at 5 mV  $s^{-1}$  and 96.0 F  $g^{-1}$  at 0.1 A  $g^{-1}$ .
- 2. FeHCF was successfully synthesized via a co-precipitation method both in the absence and presence of stabilizing agents such as trisodium citrate and potassium bitartrate. The stabilizing agents had little influence on the crystal structure or functional groups of FeHCF. The FeHCF sample synthesized without any stabilizer exhibited superior K<sup>+</sup> storage performance in aqueous electrolyte compared to that prepared with stabilizing agents, which can be attributed to reduced Ohmic resistance and improved ion diffusion. A supercapacitor assembled from FeHCF also delivered a notable areal capacitance of 1.5 mF cm<sup>-2</sup> at a current density of 5 mA cm<sup>-2</sup>, achieving a relatively high power density of 3145 μW cm<sup>-2</sup>.
- 3. NixCoyHCF materials with uniform cubic morphology and well-defined crystalline structures were successfully synthesized. Among the synthesized samples, Ni<sub>1</sub>Co<sub>2</sub>HCF exhibited the highest specific capacitance of 1068 F g<sup>-1</sup> at a current density of 1 A g<sup>-1</sup>. An aqueous hybrid supercapacitor assembled using Ni<sub>1</sub>Co<sub>2</sub>HCF delivered an areal energy density of 74.4 μWh cm<sup>-2</sup> at a power density of 750 μW cm<sup>-2</sup>, and 4.5 μWh cm<sup>-2</sup> at a high power density of 3724 μW cm<sup>-2</sup>. The device retained 87.7%

of its initial capacitance after 2000 charge–discharge cycles at a current density of 5 mA cm<sup>-2</sup>, demonstrating the excellent structural integrity and electrochemical durability of the Ni<sub>1</sub>Co<sub>2</sub>HCF material.

4. The influence of Na<sup>+</sup> incorporation on the structural characteristics and electrochemical performance of Ni<sub>3</sub>Co<sub>1</sub>HCF was systematically investigated. The introduction of Na+ ions induced slight lattice distortions and morphological changes with increased particle aggregation, while the original crystalline framework of Ni<sub>3</sub>Co<sub>1</sub>HCF was well preserved. The Na-enriched Ni<sub>3</sub>Co<sub>1</sub>HCF exhibited an excellent specific capacitance (C<sub>s</sub>) of 303.15 F g<sup>-1</sup> at a current density of 1.0 A g<sup>-1</sup>, significantly surpassing those of the Na-free analogues (Ni<sub>3</sub>Co<sub>1</sub>HCF, NiHCF, and CoHCF). This improvement is attributed to the enhanced electrochemical activity and improved ion diffusion properties of the Na-enriched material, as well as the synergistic effects between Ni and Co within the hexacyanoferrate framework. An aqueous hybrid supercapacitor assembled with Na-enriched Ni<sub>3</sub>Co<sub>1</sub>HCF delivered a high areal energy density of 166.15 μWh cm<sup>-2</sup> at a power density of 1800 μW cm<sup>-2</sup>, and retained 83.7% of its capacitance after 2000 charge–discharge cycles at 5 mA cm<sup>-2</sup>, demonstrating its excellent electrochemical reversibility and robust structural stability.

Among the investigated material systems, Ni<sub>1</sub>Co<sub>2</sub>HCF exhibited the best electrochemical performance when employed as the electrode material for supercapacitors using 2 M KOH electrolyte, whereas Na–Ni<sub>3</sub>Co<sub>1</sub>HCF demonstrated the highest electrochemical efficiency when used as the electrode material in supercapacitors with 1 M Na<sub>2</sub>SO<sub>4</sub> electrolyte.

#### NEW CONTRIBUTIONS OF THE DISSERTATION

- 1. Various hexacyanoferrate-based material systems, including CeHCF, FeHCF,  $Ni_xCo_\gamma HCF$ , and  $Na-Ni_xCo_\gamma HCF$ , were successfully synthesized. The study confirmed that all the synthesized materials exhibit intercalation-type pseudocapacitive behavior during  $K^+$  or  $Na^+$  storage in aqueous electrolytes.
- 2. The roles of the transition metals nickel and cobalt in enhancing the electrochemical performance of hexacyanoferrate-based systems were systematically investigated and highlighted. The influence of the Ni/Co ratio in Ni<sub>x</sub>Co<sub>7</sub>HCF was studied, and it was concluded that Ni<sub>1</sub>Co<sub>2</sub>HCF exhibits the highest electrochemical performance when employed in an asymmetric supercapacitor using 2 M KOH electrolyte. These findings emphasize the promising potential of mixed-metal hexacyanoferrates as high-performance electrode materials for aqueous supercapacitors.
- 3. The incorporation of Na<sup>+</sup> ions into the composition of Ni<sub>x</sub>Co<sub>γ</sub>HCF was investigated and confirmed to be an effective and simple strategy to enhance the electrochemical performance of hexacyanoferrate-based materials for aqueous Na<sup>+</sup> ion storage.

#### LIST OF PUBLISHED ARTICLES RELATED TO THE THESIS

- 1. **Vu Van Thuy**, Vu Thao Trang, Sangeun Chun, Tran Viet Thu, *Effect of surfactants on the electrochemical performance of iron hexacyanoferrate prepared by co-precipitation route for aqueous potassium-ion storage*, Journal of Nanoparticle Research, 2024. 26(4): p. 77 (a prestigious Q1 ISI-indexed journal).
- 2. **Vu Van Thuy**, Nguyen Si Hieu, Tran Viet Thu, *Novel mixed nickel/cobalt hexacyanoferrate microcubes with synergistic effects for aqueous hybrid supercapacitors*, Dalton Transactions 2024. 53(42): p. 17333-17342 (a prestigious Q1 ISI-indexed journal).
- 3. **Vu Van Thuy**, Nguyen Truong Son, Vu Hoang Ha, Le Xuan Duong, Tran Viet Thu, *Sodium-rich Nickel-Cobalt Hexacyanoferrates for Enhanced Energy Storage Performance in Aqueous Electrolyte*, New Journal of Chemistry, 2025 (a prestigious Q1 ISI-indexed journal).